

Atmospheres and UV Environments of Earth-like Planets Throughout Post-Main Sequence Evolution

Thea Kozakis, Lisa Kaltenegger

Carl Sagan Institute, Cornell University, Ithaca, NY 14853

ABSTRACT

During the post-main sequence phase of stellar evolution the orbital distance of the habitable zone, which allows for liquid surface water on terrestrial planets, moves out past the system's original frost line, providing an opportunity for outer planetary system surface habitability. We use a 1D coupled climate/photochemistry code to study the impact of the stellar environment on the planetary atmospheres of Earth-like planets/moons throughout its time in the post-main sequence habitable zone. We also explore the ground UV environments of such planets/moons and compare them to Earth's. We model the evolution of star-planet systems with host stars ranging from 1.0 to 3.5 M_{\odot} throughout the post-main sequence, calculating stellar mass loss and its effects on planetary orbital evolution and atmospheric erosion. The maximum amount of time a rocky planet can spend continuously in the evolving post-MS habitable zone ranges between 56 and 257 Myr for our grid stars. Thus, during the post-MS evolution of their host star, subsurface life on cold planets and moons could become remotely detectable once the initially frozen surface melts. Frozen planets or moons, like Europa in our Solar System, experience a relatively stable environment on the horizontal branch of their host stars' evolution for millions of years.

1. Introduction

As a star evolves, the orbital distance where liquid water is possible on the surface of an Earth-like planet, the so-called habitable zone (HZ), evolves as well. While stellar properties are relatively stable on the main sequence (MS), post-MS evolution of a star involves significant changes in stellar temperature and radius, which is reflected in the changing irradiation at a specific orbital distance during the red giant branch (RGB), and for stars massive enough ($> \sim 0.5 M_{\odot}$), the horizontal branch (HB) and the asymptotic giant branch (AGB).

To explore post-MS planetary systems for signs of life, it is critical to understand how the host star influences signs of life in the atmosphere during post-MS evolution. Not only do the host star's drastically changing temperature and luminosity change the orbital distance of the HZ, but stellar mass loss can also erode a planet's atmosphere through resulting stellar winds. The majority of studies on the habitability of rocky planets and moons have focused on planetary systems around MS stars, with only some work done on habitability around pre- and post-MS stars (see, e.g. Stern (2003); Lopez et al. (2005); Danchi & Lopez (2013); Ramirez & Kaltenegger (2014, 2016)), or stellar remnants (e.g. Wolszczan & Frail (1992); Barnes & Heller (2013); Kozakis et al. (2018)). However, no study has explored the evolution of the atmospheres and potential detectable biosignatures or UV surface environment for such post-MS planets yet.

Liquid surface water is used because it remains to be demonstrated whether subsurface biospheres, for example, under an ice layer on a frozen planet, can modify a planet’s atmosphere in ways that can be detected remotely. Although planets located outside the HZ are not excluded from hosting life, detecting biosignatures remotely on such planets should be extremely difficult (see also Ramirez (2018)). During post-MS evolution, the orbital distance of the HZ often moves out past the system’s original frost line, where water can remain in frozen form solely based on stellar irradiation at this orbital distance. In our solar system 99.99% of H₂O is located beyond the frost line (Stern 2003), presenting the opportunity for surface habitability of initially frozen planets and moons in the outer solar system during the star’s post-MS evolution.

As of now, there are tens of known gaseous planets around red giant (RG) stars (e.g. Jones et al. (2014)), although a terrestrial planet orbiting an RG has yet to be discovered. However, due to the wide separation of the post-MS HZ, such planets could be resolved via direct imaging by upcoming telescopes like the Extremely Large Telescope (ELT; see also Ramirez & Kaltenegger (2016)).

For planets orbiting post-MS stars, several studies suggest the possibility of life developing on planets orbiting subgiant or RG hosts (e.g. Lopez et al. (2005)), which strongly depends on the time required for life to evolve compared to the star’s post-MS lifetime. Ramirez & Kaltenegger (2016) have added the possibility that ice on initially frozen planets and moons could melt during the RG phase of their host stars, revealing life that initially developed under the surface.

In this study, we explore the influence of post-MS stellar irradiation on the climate, as well as its surface UV environment for Earth-like planets in the post-MS HZ. We focus on host stars with masses of 1.0 to 3.5 M_⊙, which can undergo the post-MS phase in a galaxy the age of our Milky Way. We use observed and modeled spectra of close-by RGs for our stellar models. Some of these RGs can be placed onto one evolutionary track, thus giving us first insight into a planet’s changing environment during the post-MS phase of its host star.

We first model the joint evolution of the star and the orbital distance of its post-MS HZ, along with stellar mass loss and its impacts on planetary orbital radii and atmospheric erosion following Ramirez & Kaltenegger (2016), although with an extension to higher-mass stars (1.9 to 3.5 M_⊙). We then model the atmospheres of Earth-like planets in the post-MS HZ using a 1D coupled climate/photochemistry code to explore the chemistry and UV surface environment of our model planets in the post-MS HZ. We focus on the change of atmospheric signatures that can indicate life on a planet: ozone and oxygen in combination with a reducing gas like methane or N₂O (see, e.g. the review by Kaltenegger (2017) for details). We also show climate indicators for our model planets like water and CO₂, which, in addition, can indicate whether the oxygen production can be explained abiotically. Section 2 explains our methods, Section 3 shows our results, and Sections 4 and 5 discuss and conclude our work.

2. Methods

We model the evolution of post-MS host stars and their effects on planetary orbits for 1 Earth-mass planets to calculate how long such a planet could stay within the boundaries of the post-MS HZ, as well as the effect of the host star’s evolution on the atmospheres and UV surface environment of our model planets

during the time in the post-MS HZ.

Table 1: Padova catalog stellar lifetimes

Mass (M_{\odot})	MS (Myr)	Post-MS (Myr)	RGB (Myr)	HB (Myr)	AGB (Myr)
1.0	11680	1011	851	133	27
1.3	4348	663	529	124	10
1.5	2901	294	157	125	12
1.7	1964	236	88	136	12
1.9	1409	238	52	171	15
2.0	1205	260	38	206	16
2.3	822	260	9	226	25
2.5	651	201	6	175	20
3.0	396	104	2	92	10
3.5	263	58	1	51	6

2.1. Post-MS HZ boundaries

We use stellar evolutionary tracks from the Padova catalog (Bertelli et al. 2008, 2009) that model stellar evolution from the zero-age MS (ZAMS) to the first significant thermal pulse on the AGB. All tracks used in this study have a solar-like metallicity with $Z = 0.017$ and $Y = 0.26$, from which we obtain the changing luminosity, temperature, and surface gravity, as well as the predicted time points for the beginnings of the RGB, HB, and AGB.

As shown in Table 1, the timescales for the phases of stellar evolution are highly dependent on stellar mass. While MS lifetimes are always longer for smaller masses, post-MS timescales, particularly the length of the relatively stable HB, do not linearly correlate with host mass. Stars below $2 M_{\odot}$ (0.8 to $2.0 M_{\odot}$) undergo a helium flash, which greatly increases the luminosity in the post-MS phase. Stars that do not undergo the helium flash experience a less extreme luminosity change during the RGB phase and spend a significantly higher percentage of their post-MS lifetimes on the HB. As a result, the absolute length of the HB peaks for stellar masses of $2.3 M_{\odot}$ (see Table 1 and Figure 1).

The HZ is defined as the region around one or multiple stars in which liquid water could be stable on an Earth-like rocky planet’s surface (e.g. Kasting et al. (1993); Kaltenegger & Haghhighipour (2013); Kane & Hinkel (2013)), facilitating the remote detection of possible atmospheric biosignatures. The width and orbital distance of a given HZ depend to a first approximation on two main parameters: incident stellar flux and planetary atmospheric composition. The incident stellar flux depends on the stellar luminosity and stellar spectral energy distribution, the planet’s orbital distance (semimajor axis), and the eccentricity of the planetary orbit. The warming due to atmospheric composition depends on the planet’s atmospheric makeup, energy distribution, and resulting albedo and greenhouse warming.

In the literature, very different values of stellar irradiance are used as boundaries for the HZ (see review Kaltenegger (2017)). Here we use the empirical HZ boundaries, based on the solar flux received by our neighboring rocky planets, Venus and Mars, when we can exclude liquid water on their surfaces.

This recent Venus and early Mars irradiation and the resulting HZ limits were originally defined using a 1D climate model by Kasting et al. (1993) and updated in Kopparapu et al. (2013) and Ramirez & Kaltenegger (2017, 2018) for MS stars with effective temperatures (T_{eff}) between 2,600 and 10,000 K. Note that the inner limit of the empirical HZ is not well known because of the lack of a reliable geological surface history of Venus beyond about 1 billion years due to resurfacing of the stagnant lid, which allows for the possibility of a liquid surface ocean. However, it does not stipulate a liquid ocean surface.

We calculate the flux boundaries (S_{eff}) of the post-MS HZ boundaries for the evolving stellar luminosity (Table 1) during the post-MS. Equation 1 gives a third-order polynomial curve fit of the modeling results for host stars as shown in Kaltenegger (2017), based on values derived from models by Kasting et al. (1993) and Kopparapu et al. (2013, 2014), and an extension of that work to 10,000 K by Ramirez & Kaltenegger (2018). The flux values of the HZ are defined by

$$S_{\text{eff}} = S_{\text{Sun}} + aT^* + bT^{*2} + cT^{*3} + dT^{*4}, \quad (1)$$

where $T^* = T_{\text{eff}} - 5780$, and S_{Sun} is the stellar incident values at the HZ boundaries in our solar system. Table 2 (Ramirez & Kaltenegger 2018) shows the constants a , b , c , and S_{Sun} needed to derive the stellar flux at the HZ limits valid for T_{eff} between 2,600 to 10,000 K. The inner boundaries of the empirical HZ (recent Venus), as well as an alternative inner edge limit for 3D Global Climate models (3D; Leconte et al. (2013)) and the outer limits (early Mars), are all included. The outer HZ limit in 3D and 1D models are consistent and therefore not given in separate columns in Table 2 (see e.g. Turbet et al. (2017); Wolf (2018)). However, climate models still show limitations due to unknown cloud feedback for higher stellar irradiation. Thus, we use the empirical HZ based on recent Venus and early Mars flux limits for our calculations here, even though the inner limit is uncertain, as explained before. Table 2 provides values to estimate the size of the empirical HZ, as well as models of the HZ based on 3D atmospheric models for a planet orbiting our Sun (Leconte et al. 2013) and adapted for different host stars (Ramirez & Kaltenegger 2014).

The orbital distance of the HZ boundaries around a star with luminosity L can be calculated from the incident stellar flux S_{eff} using

$$d = \sqrt{\frac{L/L_{\odot}}{S_{\text{eff}}}}, \quad (2)$$

with L measured in solar units (L_{\odot}) and the orbital distance d in astronomical units.

Table 2: HZ constants from Ramirez & Kaltenegger (2018)

Constants	Recent Venus limit (inner edge)	3D model limit (inner edge)	Early Mars (outer edge)
S_{Sun}	1.7665	1.1066	0.324
a	1.335E-4	1.2181E-4	5.3221E-5
b	3.1515E-9	1.534E-8	1.4288E-9
c	-3.3488E-12	-1.5018e-12	-1.1049E-12

2.2. Planetary semimajor axis evolution

Significant stellar mass loss occurs on the RGB and AGB, both impacting the orbital radii of orbiting planets, as well as potentially eroding planetary atmospheres. We model stellar mass loss on the RGB (\dot{M}_{RGB} in $M_\odot \text{ yr}^{-1}$) using the modified Reimers equation (Reimers 1975; Vassiliadis & Wood 1993) and the Baud & Habing (1983) parameterization for the AGB (\dot{M}_{AGB} in $M_\odot \text{ yr}^{-1}$) following Ramirez & Kaltenegger (2016),

$$\dot{M}_{RGB} = -\frac{4}{3} \times 10^{-13} \frac{L}{gR_{\text{star}}}, \quad (3)$$

$$\dot{M}_{AGB} = -\frac{4}{\times} 10^{-13} \frac{M_i}{M_{\text{star}}} \frac{L}{gR_{\text{star}}}, \quad (4)$$

where L is the stellar luminosity, g is gravity, and R is the radius, and M_i and M_{star} are the initial and current stellar mass, with everything in Solar units.

Orbital variation that will occur as a result of the host star's mass loss can be approximated as (assuming the planetary mass is negligible compared to its host's mass)

$$\frac{1}{D} \frac{dD}{dt} = -\frac{1}{M_{\text{star}}} \frac{dM_{\text{star}}}{dt}, \quad (5)$$

where D is the orbital distance. This can be integrated to obtain

$$D(t) = D_o \frac{M_i}{M_{\text{star}}(t)}, \quad (6)$$

where D_o is the initial orbital distance and M_i is the initial stellar mass. Using Equations 3 and 4 to model $M_{\text{star}}(t)$, we calculate the planet's $D(t)$ for a given D_o .

2.3. Planetary atmospheric erosion

We model planetary atmospheric erosion following Ramirez & Kaltenegger (2016) using the formalism from Canto & Raga (1991) to model planetary atmospheric erosion from stellar winds caused by mass loss. Planetary atmospheric loss per unit time (\dot{M}_a) from the stellar winds is approximated by

$$\dot{M}_a \approx -2\alpha\pi R_p^2 \rho_w v_w. \quad (7)$$

In the stellar wind flow, v_w is sound speed, ρ_w is the density, and α is the entrainment efficiency. Using the relation of

$$\dot{M}_{\text{star}} = 4\pi D^2 \rho_w v_w, \quad (8)$$

we can simplify \dot{M}_a as

$$\dot{M}_a \approx -2\alpha\pi R_p^2 \frac{\dot{M}_{\text{star}}}{4\pi D^2} \quad (9)$$

$$= -\frac{\alpha \dot{M}_{\text{star}}}{2} \left(\frac{R_p}{D} \right)^2. \quad (10)$$

Following Ramirez & Kaltenegger (2016) we use an entrainment efficiency of $\alpha = 0.2$ for our Earth-like atmospheres, assuming an Earth-mass planet with a 1 bar surface pressure. Substituting in \dot{M}_{star} from Equations 3 and 4 we calculate planetary atmospheric loss throughout the post-MS.

2.4. Post-MS stellar model spectra

The stellar input spectra consist of a combination of observed data in the UV (where models poorly represent stellar irradiation) from the *International Ultraviolet Explorer (IUE)*¹, an astronomical observatory satellite primarily designed to take UV spectra. We use type III luminosity class stars drawn from Lopez et al. (2005), Luck (2015), and Stock et al. (2018) with available long wave (LW) and short wave (SW) IUE spectra from 1216 to 3347 Å in combination with synthetic spectra from the Pickles Atlas (Pickles 1998) from 3347 to 45450 Å following Rugheimer et al. (2013). Our star sample is drawn primarily from close-by post-MS stars but includes more distant targets to allow for a more complete sample of observed IUE data for a range of post-MS stars with different spectral types, predicted masses, and evolutionary phases.

Table 3: IUE spectra hosts

Mass (M_{\odot})	Spectral Type	Star Name	Star T_{eff} (K)	Model T_{eff} (K)	Dist. (pc)	Radius (R_{\odot})	No. SW spectra	No. LW spectra	Scale factor	Evolution stage
3.0	G5 III	HD 74772	5118	5164	70.18	12.90	2	2	2.0	HB
3.0	G8 III	HD 148374	4948	5011	155.28	14.52	2	1	2.2	HB*
2.3	K0 III	β Gem	4865	4853	10.36	8.8	12	9	2.4	HB
3.0	K0 III	β Ceti	4797	4853	29.5	16.78	5	4	2.4	HB
1.3	K2 III	ι Draconis	4445	4457	31.03	11.99	1	2	2.7	HB
1.3	K2 III	θ Doradus	4320	4457	151	16	1	1	1.5	HB/AGB*
2.0	K3 III	α Boo	4286	4365	11.26	25.4	29	10	1.4	RGB
2.3	K5 III	γ Draconis	3989	4009	47.3	53.4	4	2	2.2	HB/AGB*
2.0	M5 III	γ Cru	3626	3819	27.2	84	28	11	2.2	AGB*

*Indicates that the target’s evolutionary stage was determined by H-R diagram fitting

We predict the IUE target’s original mass using H-R diagram fitting with the Padova evolutionary tracks and, if available, also use the predicted evolutionary phase from Stock et al. (2018). For stars without an estimated evolutionary phase, we use the predicted age from HR-diagram fitting (see Figure 1). Table 3 lists stellar data along with the number of SW (1150 to 1979 Å) and LW (1979 to 3347 Å) IUE spectra median-combined for each target, as well as the scale factor applied to match up the combined spectrum to the corresponding Pickles Atlas synthetic spectrum.

Figure 2 shows the spectra for the nine post-MS stars in Table 3 for a 1 AU equivalent distance from the star, where a planet would receive the same irradiation as present-day Earth.

¹<http://archive.stsci.edu/iue>

2.5. Modeling planetary atmospheres and UV surface environments

We use EXO-Prime (see, e.g. Kaltenegger (2010)), a coupled 1D radiative-convective atmosphere code based on iterations of a 1D climate model (Kasting & Ackerman 1986; Pavlov et al. 2000; Haqq-Misra et al. 2008) and 1D photochemistry model (Pavlov & Kasting 2002; Segura et al. 2005, 2007) developed for rocky exoplanets. Models simulate the effects of stellar and planetary conditions on exoplanet atmospheres and surface environments and are run to convergence following Segura et al. (2005). Model atmospheres extend to an altitude of 60 km (pressure of 1 mbar) divided up into 100 parallel planes using a stellar zenith angle of 60° . LW IR fluxes are calculated with a rapid radiative transfer model, and SW visible/near-IR fluxes are calculated with a two-stream approximation following Toon et al. (1989) with atmospheric gas scattering. The photochemistry code includes 55 chemical species with 220 reactions solved with a reverse-Euler method originally developed by Kasting et al. (1985).

We scale the incident top-of-the-atmosphere (TOA) stellar flux for our planet models to match the total integrated flux of the Sun-Earth system to compare the effects of post-MS stellar irradiance to present-day Earth. Planetary outgassing rates are kept constant for H_2 , CH_4 , CO , N_2O , and CH_3Cl and maintain constant mixing ratios of O_2 at 0.21 and CO_2 at 3.55×10^{-6} , while N_2 concentrations vary to reach the initial surface pressure model condition (following Segura et al. (2003, 2005); Rugheimer et al. (2013, 2015,b); Rugheimer & Kaltenegger (2018); Kozakis et al. (2018)).

Many reactions in Earth’s atmosphere are driven by the Sun’s UV flux. Some atmospheric species exhibit noticeable features in our planet’s spectrum as a result directly or indirectly of biological activity. Oxygen or ozone in combination with a reducing gas like methane are currently our best biosignatures, indicating biological activity on a temperate rocky planet (see review Kaltenegger (2017)). Ozone (O_3) is

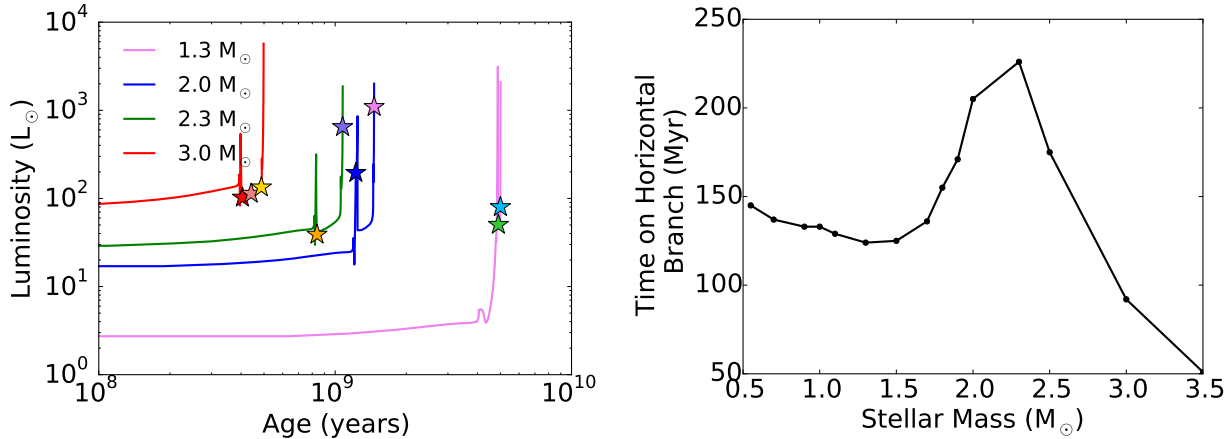


Fig. 1.— (Left) Post-MS IUE targets (marked as stars) fit to the Padova evolutionary tracks and (right) the length of the HB for each specific mass track. More information on targets shown in Table 3.

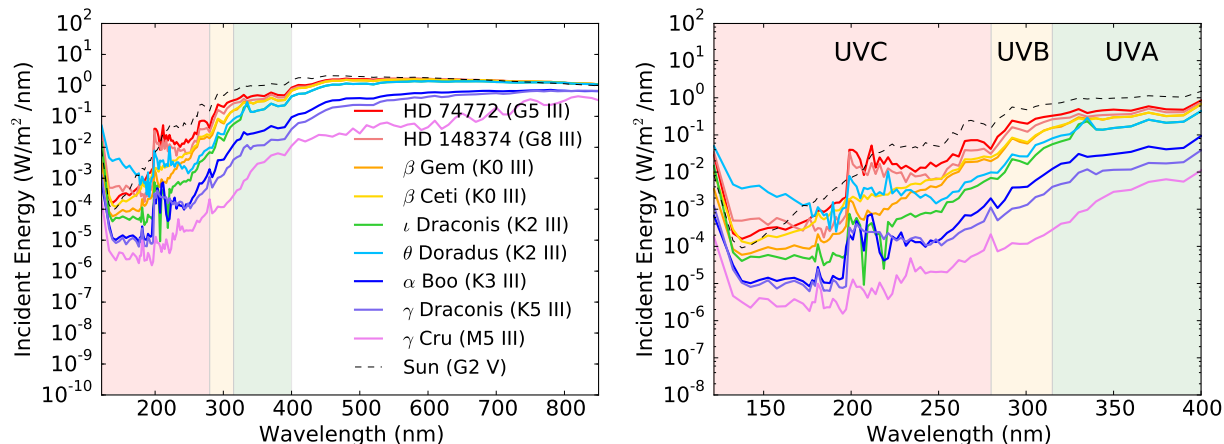
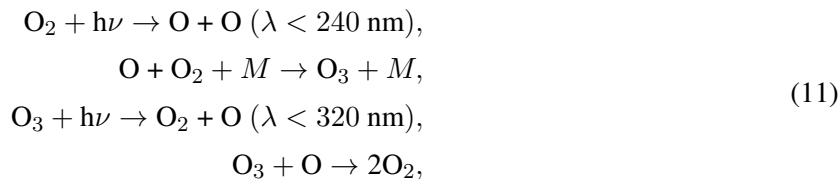


Fig. 2.— Red giant spectra scaled to the Earth-irradiation based on a combination of IUE data and Pickles model spectra for our grid stars (Table 3). The UV irradiation present-day Earth receives from the Sun (G2 V) is shown as a black dotted line.

created and destroyed with UV photons through the Chapman reactions (Chapman 1930),



where M is a background molecule such as N_2 . These reactions are primarily responsible for ozone production on present-day Earth and are dependent on the UV portion of the stellar host’s spectrum.

In addition, atmospheric ozone levels determine the amount of UV flux that reaches the planetary surface on present-day Earth (see, e.g. Rugheimer et al. (2015); O’Malley-James & Kaltenecker (2017); Kozakis et al. (2018)), which can impact surface life. We focus here in particular on UVB (280-315 nm) and UVC (100-280 nm). UVB irradiation, which can be damaging for surface life, is partially shielded by ozone, whereas UVC irradiation, which is energetic enough to cause DNA damage, is almost entirely shielded by ozone, along with being the primary source that creates ozone. We explore the UV environment on the surface of our model planets following Rugheimer et al. (2015), O’Malley-James & Kaltenecker (2017), and Kozakis et al. (2018) and compare it to present-day Earth’s.

3. Results

3.1. Orbital distance of the post-MS HZ

We modeled the orbital distance of the post-MS HZ for host stars of 1.0 to $3.5 M_\odot$. Then we calculated the initial semimajor axis required for a planet to spend the maximum amount of time in the post-MS HZ while undergoing semimajor axis evolution (see Equation 6). Post-MS stars that undergo a helium flash (0.8 to $2 M_\odot$) sustain significantly larger luminosity increases (factors of order 1000) when compared to

higher-mass stars that do not experience helium flashes (factors of order 100). As a result, planets around lower-mass stars are subject to larger amounts of semimajor axis variation due to higher stellar mass-loss rates.

Table 4 shows the factor by which stellar luminosity increases on the post-MS, the post-MS HZ boundaries for the beginning and end points of the HB (the most stable part of the post-MS), and the semimajor axis evolution of the orbit of a planet that could spend the maximum possible time in the post-MS HZ. Post-MS HZ orbital distances are comparable for lower-mass stars (1.0 and 1.3 M_{\odot}) and higher-mass stars (2.0 and 2.3 M_{\odot}) due to the much higher luminosity increase for our grid stars that undergo helium flashes ($< 2 M_{\odot}$). Greater luminosity increases during the post-MS additionally cause higher stellar mass-loss rates (Equations 3 and 4), which, in turn, cause larger variations in an orbiting planet’s semimajor axis for our lower-mass grid stars (Equation 6).

Table 4: HZ boundaries and semimajor axis evolution

Track Mass (M_{\odot})	L factor increase	HB start (AU)		HB end (AU)		Semimajor axis* (AU)		
		Inner HZ	Outer HZ	Inner HZ	Outer HZ	Initial	HB start	HB end
1.0	4457	5.1	12.7	5.6	13.9	10.0	12.3	12.3
1.3	1258	5.6	14.0	12.0	31.0	12.5	13.8	13.9
2.0	126	5.2	12.6	12.2	31.0	12.2	12.3	12.3
2.3	68	5.0	12.0	10.5	26.4	12.0	12.0	12.0
3.0	74	7.5	18.3	13.3	33.3	18.2	18.2	18.2
3.5	73	10.5	25.6	14.7	36.7	25.0	25.0	25.0

*Semimajor axis values correspond to the orbit that spends the maximum amount of time in the post-MS HZ

3.2. Post-MS habitable zone lifetime

For the modeled post-MS HZs and orbital evolution of 1 Earth-mass planets for stars of masses 1.0 to 3.5 M_{\odot} , we explore the longest time a planet can orbit within the post-MS HZ. We also estimate the resulting planetary atmosphere erosion due to the host star’s mass loss (see Table 5). Note that the longest time spent in the post-MS HZ does not need to be continuous due to the host stars changing luminosity in the post-MS phase. Thus, we distinguish between the time an Earth-mass planet can spend continuously in the post-MS HZ (post-MS CHZ), and the maximum time a planet can spend in the post-MS HZ that is not continuous and can put the planet in a temporary runaway greenhouse state due to the large increase of stellar luminosity during the peak of the RGB (see Figure 3 and discussion).

A star with a ZAMS mass of 1.0 M_{\odot} has a total lifetime of 12.7 Gyr, spending only 8% of its life on the post-MS with 851 Myr on the RGB, 133 Myr on the HB, and 27 Myr on the AGB. The initial semimajor axis for a planet leading to the maximal time in the post-MS HZ is 10.0 AU. It spends 66 Myr in the post-MS HZ on the RGB, 22 Myr outside of the post-MS HZ during the RGB peak, where stellar irradiation exceeds the empirical HZ limits, and then remains in the post-MS HZ for 153 Myr on the HB. The stellar irradiation exceeds the empirical HZ limits again during the AGB. Stellar winds erode about 10% of the planet’s original atmosphere when its star’s irradiation exceeds the empirical HZ limits during the AGB.

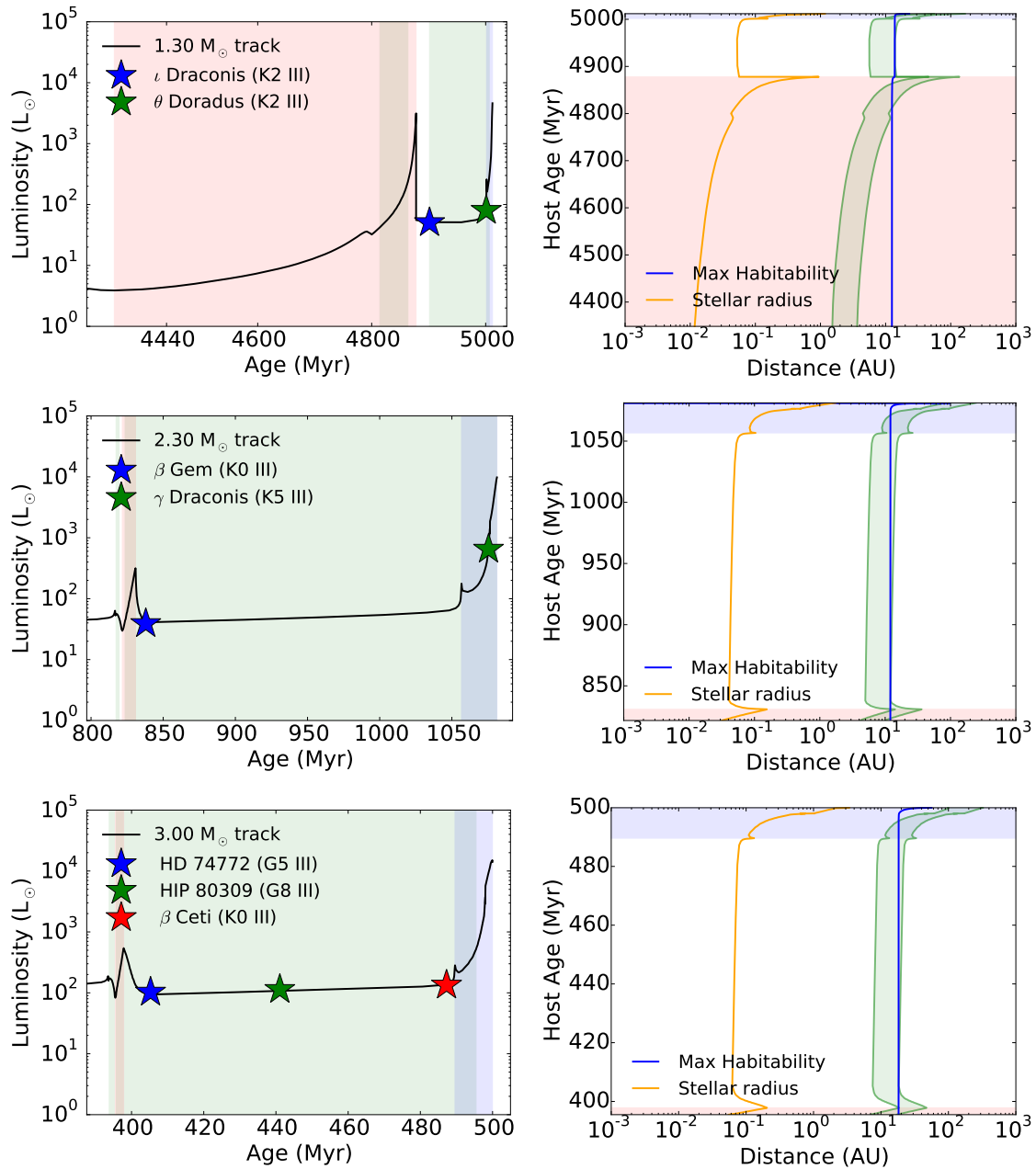


Fig. 3.— (Left) Stellar luminosity versus stellar age during the post-MS with grid stars indicated on the evolutionary track with stars, and (right) evolution of the orbital distances of the post-MS HZ for (top) a 1.3, (middle) a 2.3, and (bottom) a 3.0 M_{\odot} track star. For the plots on the left the red zone indicates the RGB, the blue zone the AGB, and the green zone the time that the model planet passes through the HZ. The points of evolution modeled in Section 3.4 are marked with stars. For plots on the right the green zone indicates the changing orbital distance of the HZ, the orange line the evolution of the host star’s radius, and the blue line the orbital evolution of an Earth-sized planet spending the maximum amount of time in the HZ.

A star with a ZAMS mass of $1.3 M_{\odot}$ has a total lifetime of 5.0 Gyr, spending 13% of its life on the post-MS with 529 Myr on the RGB, 124 Myr on the HB, and 10 Myr on the AGB. The initial semimajor axis for a planet leading to the maximum amount of time in the post-MS HZ is 12.5 AU. It spends 49 Myr in the post-MS HZ on the RGB, 38 Myr outside of the post-MS HZ during the RGB peak, where stellar irradiation exceeds the empirical HZ limits, and then remains in the post-MS HZ for 105 Myr on the HB and the beginning of the AGB. Stellar winds erode about 5% of the planet’s original atmosphere when its star’s irradiation exceeds the empirical HZ limits during the AGB.

Table 5: Post-MS HZ lifetime

Track Mass (M_{\odot})	Total post- MS (Myr)	Max HZ (Myr)	Max CHZ (Myr)	Time outside HZ ¹ (Myr)	Atmosphere Eroded (%)
1.0	1011	219	153	22	10
1.3	663	154	105	38	5
2.0	260	191	163	50	1
2.3	260	259	257	4	0.1
3.0	104	101	97	1	0.01
3.5	58	56	56	0	0.1

*Planetary parameters are those of the orbit of maximum time in the HZ

¹ Time spent outside of the HZ during the RGB after initially entering HZ

A star with a ZAMS mass of $2.0 M_{\odot}$ has a total lifetime of 1.5 Gyr, spending 18% of its life on the post-MS with 38 Myr on the RGB, 206 Myr on the HB, and 16 Myr on the AGB. The initial semimajor axis for a planet leading to the maximum amount of time in the post-MS HZ is 12.2 AU. It spends 28 Myr in the post-MS HZ on the RGB, 50 Myr outside of the post-MS HZ during the RGB peak, where stellar irradiation exceeds the empirical HZ limits, and then remains in the post-MS HZ for 163 Myr on the HB. Stellar winds erode about 1% of the planet’s original atmosphere when its star’s irradiation exceeds the empirical HZ limits during the AGB.

A star with a ZAMS mass of $2.3 M_{\odot}$ has a total lifetime of 1.08 Gyr, spending 24% of its life on the post-MS with 9 Myr on the RGB, 226 Myr on the HB, and 25 Myr on the AGB. The initial semimajor axis for a planet leading to the maximum amount of time in the post-MS HZ is 12.0 AU. It spends 2 Myr in the post-MS HZ on the RGB, 4 Myr outside of the post-MS HZ during the RGB peak, where stellar irradiation exceeds the empirical HZ limits, and then remains in the post-MS HZ for 257 Myr on the HB and the beginning of the AGB. Stellar winds only erode 0.1% of the planet’s original atmosphere when its star’s irradiation exceeds the empirical HZ limits during the AGB.

A star with a ZAMS mass of $3.0 M_{\odot}$ has a total lifetime of 500 Myr, spending 21% of its life on the post-MS with 2 Myr on the RGB, 92 Myr on the HB, and 6 Myr on the AGB. The initial semimajor axis for a planet leading to the maximum amount of time in the post-MS HZ is 18.2 AU. The planet spends a total of 4 Myr in the post-MS HZ on the RGB, 1 Myr outside of the post-MS HZ when stellar irradiation exceeds the empirical HZ limits during the RGB peak, and then remains in the post-MS HZ for 97 Myr on the HB and the beginning of the AGB. Stellar winds only erode 0.01% of the planet’s original atmosphere when its stars irradiation exceeds the empirical HZ limits during the AGB, due to the wide orbital separation and the brevity of the star’s lifetime in our model.

A star with a ZAMS mass of $3.5 M_{\odot}$ has a total lifetime of 321 Myr, spending 18% of its life on the

post-MS with 1 Myr on the RGB, 51 Myr on the HB, and 6 Myr on the AGB. Due to a smaller overall luminosity change for stars this massive, a continuous post-MS HZ (CHZ) for a planet exists. The initial semimajor axis for a planet leading to the maximum amount of time of 56 Myr in the post-MS HZ is 25 AU from the RGB to the AGB. Stellar winds erode about 0.1% of the planet’s original atmosphere when its star’s irradiation exceeds the empirical HZ limits during the AGB, despite the large semimajor axis because of prolonged exposure to high stellar mass-loss rates on the AGB.

3.3. Planets at Earth-equivalent orbital distances

We modeled atmospheres of Earth-like planets at distances where they receive the same integrated flux as present-day Earth ($S_{\text{eff}} = 1$) with surface pressures of 1.0 bar. We focus on the change of atmospheric signatures that can indicate life on a planet, ozone and oxygen in combination with a reducing gas like methane or N_2O , as well as climate indicators such as water and CO_2 , which can also indicate whether the oxygen production can be explained abiotically (see review Kaltenecker (2017)). We also explore the amount of UV flux reaching the model planetary surface in the post-MS HZ throughout the host star’s evolution later in Section 3.4. The temperature and mixing ratios of the resulting model atmospheres are shown for all planet models for our our grid stars in Figure 4, with present-day Earth’s profiles shown as black dashed lines for comparison.

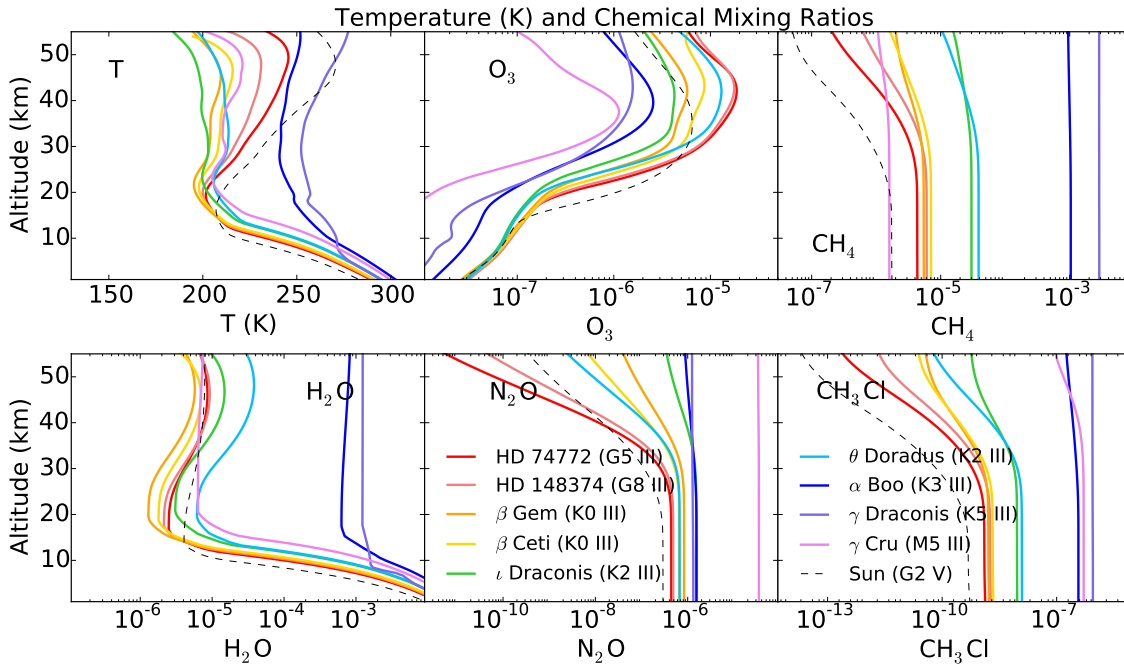


Fig. 4.— Temperature and atmospheric mixing ratio profiles for an Earth-like planet orbiting our grid post-MS stars at the Earth-equivalent distance.

As a star expands and cools during the post-MS phase, the peak of the stellar spectrum shifts to redder

wavelengths, which heat planetary surfaces more efficiently for Earth-like planets with a mostly $\text{N}_2\text{-H}_2\text{O-CO}_2$ atmosphere (see e.g. Kasting et al. (1993)). This is partly due to the effectiveness of Rayleigh scattering, which decreases at longer wavelengths. A second effect is the increase in NIR absorption by H_2O and CO_2 as the star’s spectral peak shifts to these wavelengths, meaning that the same integrated stellar flux that hits the top of a planet’s atmosphere from a cool red star warms a planet more efficiently than the same integrated flux from a star with a higher effective surface temperature. This causes planetary surface temperatures to be lower for planets orbiting hotter stars than cooler stars, even with the same amount of total integrated incident flux, as shown in Figure 4 and Table 6.

Note that due to the drop in stellar temperature during expansion on the RGB, the average surface temperature of a post-MS star is lower than for MS stars with similar masses. All grid stars in our study have lower effective temperatures than the Sun, and as a result, all calculated surface temperatures for planets receiving Earth-like irradiation are higher than present-day Earth’s (shown as a dashed black line), ranging from 1.1 K for the hottest to 18.2 K higher for the coolest post-MS grid star.

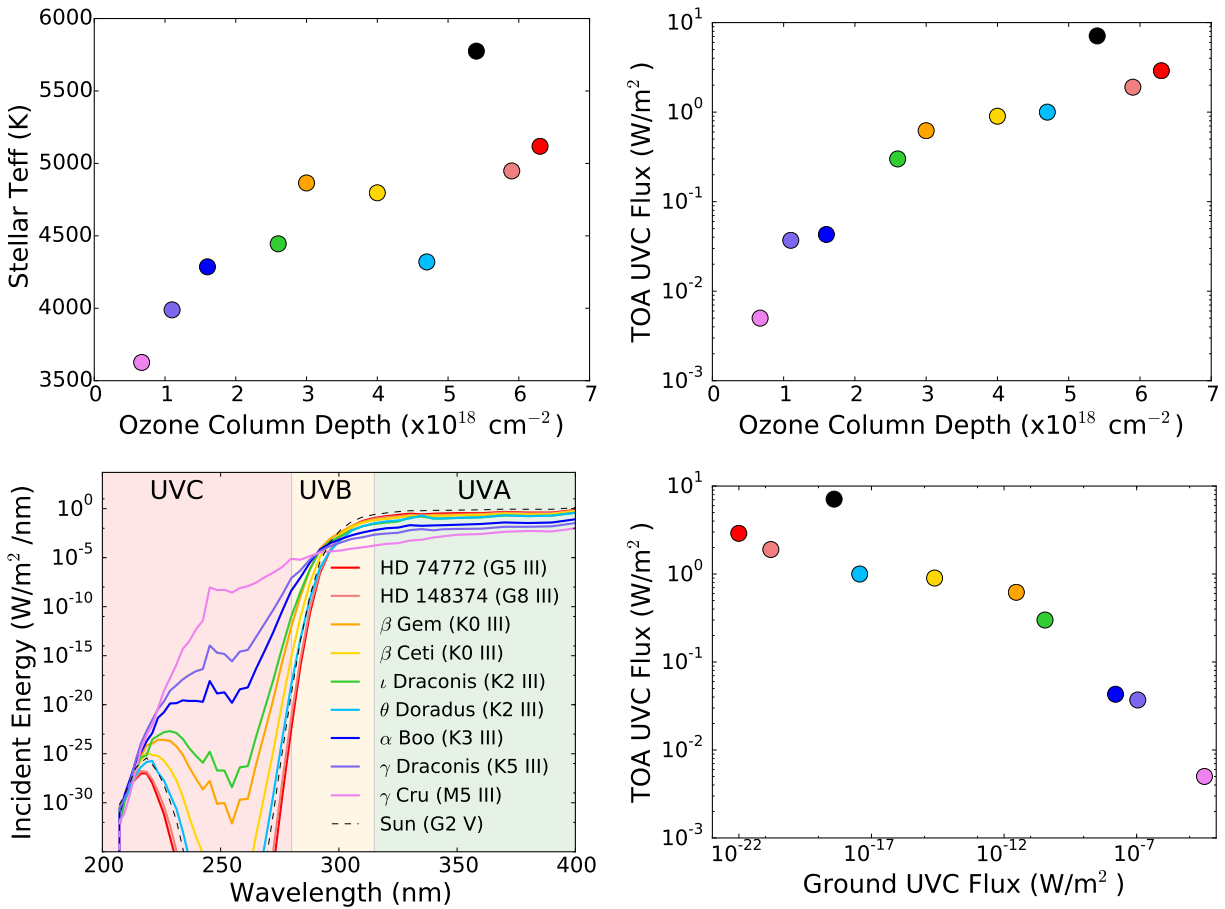


Fig. 5.— (Top, left) Incident top of the atmosphere (TOA) integrated UVC flux versus post-MS grid stars effective temperature, (bottom, left) ground UV flux shown as a function of wavelength for Earth-like planet models, (top, right) TOA integrated UVC flux versus total ozone column depth, and (bottom, right) TOA integrated UVC flux versus ground integrated UVC flux. The different colored dots/lines indicate individual post-MS grid host stars for the planet model, the black dots/line shows present-day Earth for comparison.

Planets orbiting cooler stars in the HZ can receive lower levels of UV flux (see Figure 2), impacting ozone production rates. As seen in Equation 11 ozone creation requires short-wavelength UV photons ($\lambda < 240$ nm), resulting in larger amounts of ozone for planets experiencing higher amounts of incident UVC ($100 \text{ nm} < \lambda < 280 \text{ nm}$). Since our target stars all have lower UVC radiation than the Sun, model atmospheres at the Earth-equivalent distance tend to have lower ozone production rates, resulting in smaller ozone column depths (Table 6 and Figure 5). The calculated ozone column depth of the planet orbiting in the HZ of the coolest grid star is only 11% of the hottest grid host star planet in the HZ, and 12% of the column depth on present-day Earth.

This lower amount of incident UV flux causes lower photolysis rates in the upper atmosphere, with planets orbiting cooler stars experiencing less photolysis-related depletion (see Figure 4). This effect is particularly relevant for CH_4 , N_2O , and CH_3Cl , which are also heavily depleted via reactions with OH, a by-product of ozone photolysis. The comparable/higher levels of these species should maintain the detectability of both gases in combination as a sign of biological activity on a planet. Our post-MS model planet photochemistry profiles are consistent with studies of cooler MS stars (e.g. Segura et al. (2005); Rugheimer et al. (2013, 2015)).

Table 6: Model Summary for Earth-Equivalent Distances

Spectral Type	Star Name	Stellar T_{eff} (K)	Surface T_{eff} (K)	UVB TOA W/m^2	UVC TOA W/m^2	Ozone Column Depth (cm^{-2})
G2 V	Present-day Earth	5775	288.2	18.9	7.1	5.4×10^{18}
G5 III	HD 74772	5118	289.3	8.3	2.9	6.3×10^{18}
G8 III	HD 148374	4948	294.5	5.8	1.9	5.9×10^{18}
K0 III	β Gem	4865	295.0	3.1	0.62	3.0×10^{18}
K0 III	β Ceti	4797	295.5	3.2	0.90	4.0×10^{18}
K2 III	ι Draconis	4445	298.6	0.96	0.30	2.6×10^{18}
K2 III	θ Doradus	4320	299.1	1.4	1.0	4.7×10^{18}
K3 III	α Boo	4286	303.6	0.19	0.043	1.6×10^{18}
K5 III	γ Draconis	3989	304.7	0.063	0.037	1.1×10^{18}
M5 III	γ Crucis	3626	306.4	0.0054	0.0050	6.7×10^{17}

Table 6 shows the TOA integrated flux for UVB and UVC at the 1 AU-equivalent distance, as well as the resulting ozone column depth and average surface temperature for Earth-like planetary models with 1 bar surface pressure. It also shows present-day Earth values for comparison in the first line.

The UV ground fluxes vary drastically as a function of wavelength due to the wavelength-dependent nature of ozone-shielding effectiveness. Because we use observed UV data for our grid stars, and these stars are at different stages in their post-MS evolution, the correlation between effective temperature and UVC flux is not exact (see all UV fluxes in Table 7). However, the correlation between ozone column depth and UVC surface irradiation is clearly shown in Figure 5.

Although planets with cooler post-MS host stars generally have lower levels of incident UVC flux, the lower amounts also decrease ozone production, allowing a higher percentage of UVB and UVC radiation to reach their surfaces compared to planets orbiting post-MS stars with higher incident UVC flux. The differences in the attenuation percentage are most significant for UVC flux, which is almost entirely shielded

by ozone. As seen in Figure 5 higher incident UVC flux correlates with higher ozone column depth and lower ground UVC as a result of ozone shielding. Note that both β Ceti and θ Doradus have high UVC flux compared to the grid stars with similar surface temperature, and H-R diagram fitting matches both stars to a later stage in the post-MS evolution. All model planets for post-MS host stars with lower effective temperatures than the Sun show higher UVC surface levels than present-day Earth, with model planets orbiting cooler post-MS hosts generally experiencing higher levels of surface UVC than similar planets orbiting hotter post-MS hosts (see Table 7).

Table 7: UV Integrated Fluxes for Earth-Equivalent Distances

Spectral Type	Star Name	UVB 280 - 315 nm (W/m ²)			UVC 121.6 - 280 nm (W/m ²)		
		ITOA	Ground	% to ground	ITOA	Ground	% to ground
G2 V	Present day Earth	18.9	2.2	11	7.1	3.9E-19	5.4E-18
G5 III	HD 74772	8.3	0.92	11	2.9	9.9E-23	3.4E-21
G8 III	HD 148374	5.8	0.76	13	1.9	1.6E-21	8.4E-20
K0 III	Pollux	3.1	0.69	22	0.62	2.9E-12	4.7E-10
K0 III	β Ceti	3.2	0.59	19	0.90	2.4E-15	2.7E-13
K2 III	ι Draconis	0.96	0.26	27	0.30	3.5E-11	1.2E-8
K2 III	θ Doradus	1.4	0.27	19	1.0	3.6E-18	3.4E-16
K3 III	α Boo	0.19	0.065	34	0.043	1.6E-8	3.6E-5
K5 III	γ Draconis	0.063	0.023	37	0.037	3.1E-7	0.00084
M5 III	γ Crucis	0.0054	0.0025	46	0.0050	3.6E-5	0.71

3.4. Planetary Atmospheres: post-MS evolution

To explore a planet’s characteristics while orbiting an evolving post-MS star, we model the same planet at different points along its host star’s stellar evolution. We include the increase of the initial semimajor axis of the planet, which evolves outward with stellar mass loss (see Section 3.1). We model planets orbiting post-MS host stars on three different mass tracks, with which we can match our observed post-MS grid stars to specific stellar masses and evolutionary phases (see Table 3). The temperature and photochemical profiles of our model planets are shown in Figure 6, a summary of the results is shown in Table 8, and the UV surface flux data are summarized in Table 9 and compared to present-day Earth.

Table 8: Model Summary throughout post-MS evolution

Star Name	Track Mass (M_{\odot})	Evolutionary Stage	Semimajor Axis (AU)	S_{eff}	Surface Pressure (bar)	Ozone Column Depth cm ⁻²
ι Draconis	1.3	HB	13.8	0.2689	0.95	5.1E+18
θ Doradus	1.3	HB/AGB	13.8	0.5507	0.95	1.19E+19
β Gem	2.3	HB	12.0	0.2835	1.0	3.2E+18
γ Draconis	2.3	HB/AGB	12.1	1.0647	0.99	2.5E+18
HD 74772	3.0	HB I	18.2	0.2824	1.00	5.3E+19
HD 148374	3.0	HB II	18.2	0.3239	1.00	7.4E+18
β Ceti	3.0	AGB	18.23	0.4095	1.00	4.1E+18

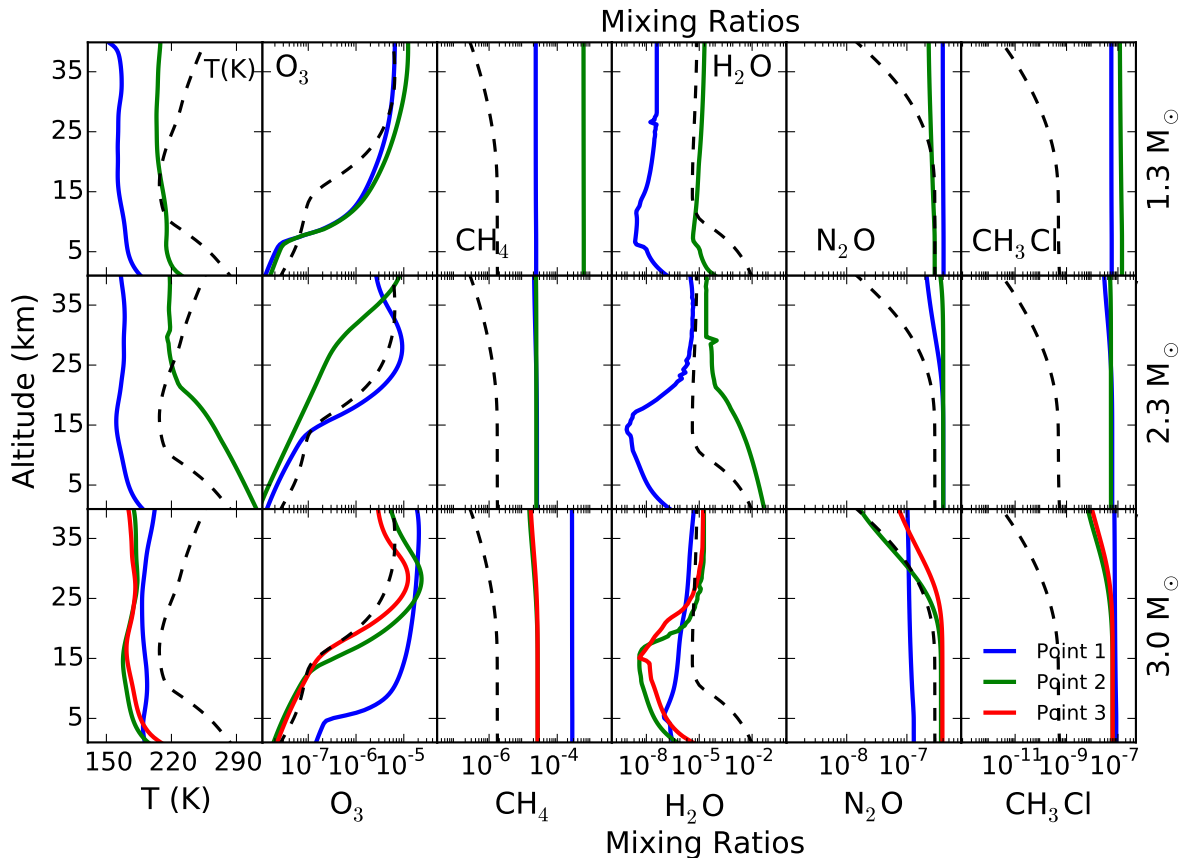


Fig. 6.— Evolving temperature and photochemical profiles of Earth-like planets orbiting post-MS host stars on 1.3 (top), 2.3 (middle), and 3.0 (bottom) mass tracks. Blue lines represent the first point in evolution sampled, green lines the second, and for the 3.0 M_{\odot} track red lines the third.

Planets that would spend the maximum overall time in the post-MS HZ orbit initially near the outer edge of the post-MS HZ, warming with increasing incident stellar flux as the luminosity of the post-MS host increases. Note that at the outer edge of the post-MS HZ, planets initially experience similar to lower levels of UVC flux than present-day Earth, producing slightly lower amounts of ozone. Although less ozone shielding exists, the lower incident flux produced UV surface environments comparable to present-day Earth for most of our models (Figure 6 and Table 8). These model atmospheres produce similar to slightly lower amounts of ozone but higher amounts of methane than on present-day Earth. The N_2O levels are similar, while CH_3Cl levels are similar to slightly higher for these post-MS planetary atmospheres. For the 1.3 M_{\odot} case there is a slight decrease in UV to the ground from the first to second point in evolution sampled due to an increase in incident UV causing higher ozone production rates. There is an increase of UV to the ground over time for the 2.3 and 3.0 M_{\odot} cases resulting from lower amounts of incident UV causing less ozone shielding (see Table 9).

Unlike the profiles shown in Figure 4 for models at the Earth-equivalent distance, these models are mainly near the outer edge of the post-MS HZ and have lower incident UV flux and therefore lower amounts

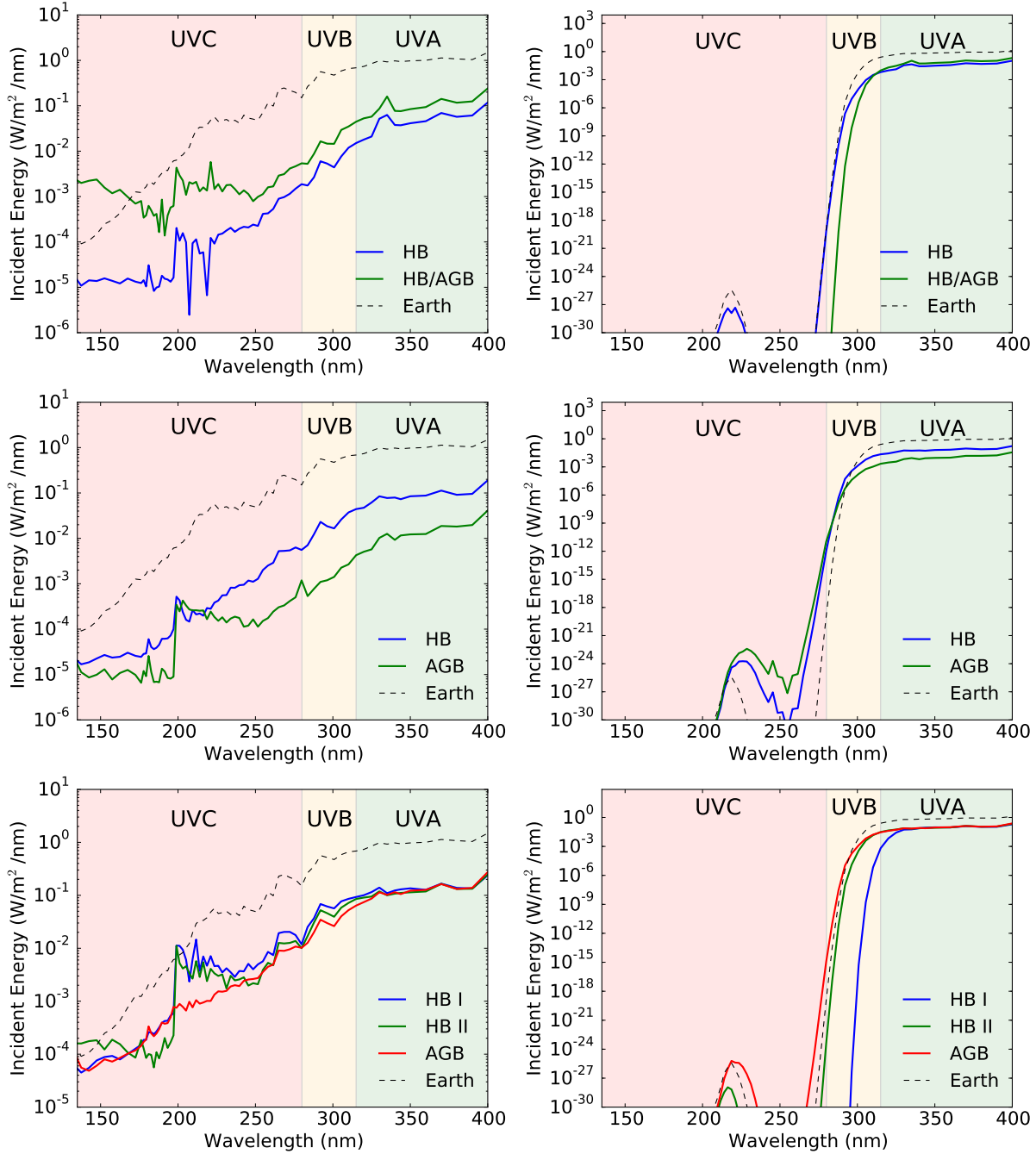


Fig. 7.— Top of the atmosphere and surface UV fluxes for Earth-like planets in the post-MS HZ orbiting post-MS stars. We mimic their host stars evolution by using known stars matched to different parts of their post-MS evolution as marked in Figure 3.

of upper atmosphere photolysis (Figure 6). This is most evident in the nearly vertical profiles of the species most sensitive to photolysis and its products: CH_4 , N_2O , and CH_3Cl .

Table 9: UV Integrated Fluxes throughout Post-MS Evolution

Star Name	Mass (M_{\odot})	UVB 280 - 315 nm (W/m^2)			UVC 121.6 - 280 nm (W/m^2)		
		ITOA	Ground	% to ground	ITOA	Ground	% to ground
Present day Earth	1.0	18.9	2.2	11	7.1	3.9E-19	5.4E-18
ι Draconis	1.3	0.26	0.052	20	0.081	2.1E-19	2.6E-16
θ Doradus	1.3	0.79	0.062	7.8	0.58	3.6E-31	6.3E-29
β Gem	2.3	0.87	0.22	25	0.18	3.7E-12	2.1E-9
γ Draconis	2.3	0.067	0.020	30	0.039	5.0E-11	1.3E-7
HD 74772	3.0	2.3	0.0033	0.14	0.82	2.5E-46	3.0E-44
HD 148374	3.0	1.9	0.25	13	0.60	1.3E-23	2.1E-21
β Ceti	3.0	1.3	0.27	21	0.37	7.7E-15	2.1E-12

4. Discussion

4.1. How could life form/become detectable on objects habitable during the post-MS?

It is uncertain how long life needs to emerge and evolve, with estimates ranging from 0.5 to 1 Gyr (see, e.g. Furnes et al. (2004); Lopez et al. (2005)). However, even if post-MS HZ timescales would be too short for the development of life, increasing luminosity during the RGB phase should melt the initially frozen surfaces of moons and planets, revealing subsurface life (Ramirez & Kaltenegger 2016). Frozen planets and moons are not excluded from hosting life; however, it is unknown whether subsurface biospheres—for example, under an ice layer on a frozen planet—can modify a planet’s atmosphere in ways that can be detected remotely. Thus, we concentrate on the liquid water zone in our paper.

4.2. Could we directly image planets in the post-MS HZ of RGs?

Upcoming ground-based ELTs are also designed to characterize exoplanets. Even though a post-MS host star is very bright compared to an MS star, the wider separation of the post-MS HZ when compared to an MS star’s HZ also opens up the possibility of directly imaging planets in the post-MS HZ for close-by systems (see Lopez et al. (2005); Ramirez & Kaltenegger (2016)). To further explore this idea, we have compiled a list of post-MS luminosity class III stars within 30 pc and indicate whether these stars have available IUE data (see Table 10). We compiled this target list using several published lists (Lopez et al. 2005; Luck 2015; Stock et al. 2018) and updated their distances using *Gaia* DR2 data (Gaia Collaboration et al. 2016).

Comparing the angular separation (θ (arcsec) = a (AU) / d (pc); where a = planet semi-major axis, d = distance to star system) for the angular separation of the 1 AU equivalent distance (Table 10) with the inner working angle (IWA) for a telescope, which describes the minimum angular separation at which a faint object can be detected around a bright star, we can determine whether planets at such orbital distances could be remotely detected and resolved in the near future. For example, the 38 m diameter Extremely Large Telescope should have an IWA of about 6 milliarcseconds (mas) when observing in the visible region of the spectrum (assuming θ IWA $\approx 2(\lambda D)$, where λ is the observing wavelength and D is the telescope diameter).

Table 10: Luminosity class III stars within 30 pc

Mass (M_{\odot})	Spectral Type	Star Name	IUE data ¹	Stellar T_{eff} (K)	Distance (pc)	Radius (R_{\odot})	1 AU equiv. (AU)	Ang. Sep. ($''$)	Post-MS (Myr)	HB (Myr)
2.0*	K1.5 III	α Boötis	B	4286	11.3	25.4	13.98	1.24	260	206
2.0*	M3.5 III	γ Crucis	B	3626	27.2	84	33.08	1.22	260	206
1.3	K5 III	α Tauri	N	3910	20.5	44.13	20.21	0.99	633	124
2.3*	K0 III	β Gem	B	4865	10.4	8.8	6.24	0.60	260	226
1.7	K2 III	α Arietis	S	4480	20.2	14.9	8.96	0.44	236	136
2.5	K0 III	θ Centauri	S	4980	18.0	10.6	7.87	0.44	201	185
3.0*	K0 III	β Ceti	B	4797	29.5	16.78	11.57	0.39	104	92
1.5	K2.5 III	ϵ Scorpii	S	4560	23.2	12.6	7.85	0.34	294	125
2.3	K0 III	γ^2 Sagittarii	S	4769	24.9	12	8.17	0.33	260	226
1.9	K0 III	ϵ Cygni	N	4710	23.2	10.82	7.19	0.31	238	171
3.0	G8 III	η Draconis	S	5055	27.3	11	8.42	0.31	104	92
1.3	K2 III	β Ophiuchi	S	4467	24.4	12.42	7.42	0.30	663	124
1.5	K2 III	κ Ophiuchi	S	4529	27.2	11	6.76	0.25	294	125
1.5	K2 III	β Columbae	N	4545	27.8	11.5	7.12	0.26	294	125
1.8	A7 III	γ Boötis	S	7800	26.7	3.34	6.09	0.23	157	155
1.7	K0 III	ν Octantis	S	4860	19.4	5.81	4.11	0.21	236	136
1.3	K1 III	ν^2 CMa	S	4790	19.8	4.9	3.37	0.17	663	124
1.8	A5 III	111 Her	N	8153	28.3	1.83	3.64	0.13	157	155

¹Key for the IUE data: N = no data, S = short wave data, B = both short wave and long wave data.

*Indicates that target is modeled in this paper

Table 10 shows the angular separation of their 1 AU equivalent orbital distance to compare them to predicted IWAs for ground-based telescopes like the ELT with a proposed IWA of 6 milliarcseconds (Quanz et al. 2015). Note that we excluded binary systems and variables from our list. The angular separation of the 1 AU equivalent orbital distance during the post-MS for nearby RGs ranges from 1.2 to 0.2 arcseconds, making such observations interesting for upcoming ground-based direct imaging surveys.

4.3. Continuous time in the HZ

Note that Table 5 shows two values for the maximum time a planet orbiting a post-MS host star can stay in the HZ: the time a planet can stay continuously in the post-MS CHZ and a longer time period that consists of the sum of the time a planet can spend in the HZ during a star’s post-MS evolution. The sum of time a planet can spend in the post-MS HZ is interrupted by the times a planet receives higher luminosity, which should put it into a runaway greenhouse state (see, e.g. Kasting et al. (1993)), where a planet would boil off surface water and subsequently would lose hydrogen to space. Estimates of the time such water loss would take vary (see, e.g. Kasting et al. (1993); Kopparapu et al. (2013)). Whether such a runaway greenhouse would be reversible if the irradiation of the star decreases during the HB phase is unclear and will depend on many factors, including cloud feedback during the onset of the runaway greenhouse stage, which is unknown and will only be constrained once atmospheric observations of such planets are available. Thus, Table 5 shows both values.

4.4. Comparisons to previous studies

Earlier studies have explored the post-MS HZ boundaries and evolution (e.g. Ramirez & Kaltenegger (2016); Danchi & Lopez (2013); Stern (2003)), however, they did not explore planetary climate and UV surface environments on planets in the post-MS HZ. Here we compare our results of post-MS HZ boundary evolution to earlier studies. Note that Ramirez & Kaltenegger (2017, 2018) have expanded the HZ concept to stars with higher surface temperatures, which allows an extension of post-MS HZ calculations to higher-mass stars. We calculate post-MS HZ limits, stellar mass-loss rates, and planetary semimajor axis evolution following Ramirez & Kaltenegger (2016), and find consistent results for the overlapping mass range between the two studies (1.0 to 1.9 M_{\odot}). Stern (2003) calculates temperate distances and habitability timescales for 1 to 3 M_{\odot} post-MS stars, both of which are consistent with our HZ limits. We also find multiple periods of habitability for a range of semimajor axes during the post-MS, as noted by Danchi & Lopez (2013).

5. Conclusions

We explore how long planets could remain in the post-MS HZ for post-MS stars from 1.0 to 3.5 M_{\odot} . We additionally study how the stellar environment would affect the atmospheric composition and potentially detectable biosignatures, as well as the surface UV conditions of Earth-mass planets. We model atmospheric erosion and semimajor axis evolution resulting from stellar winds/mass loss.

Less massive grid stars that do undergo a helium flash ($< 2 M_{\odot}$) experience a larger luminosity increase during the post-MS (Table 4) causing a more drastic change in the orbital distance of the post-MS HZ compared to the MS HZ, as well as higher stellar mass-loss rates and semimajor axis variation. We find that the maximum time a planet can spend in the post-MS HZ is between 56 and 257 Myr, for our grid stars, which is highly dependent on the amount of time the host star spends on the relatively stable HB. The wide orbital separation of the post-MS HZ limits atmospheric erosion in our model to about 10% of the initial atmosphere for Earth-like planets with 1 bar surface pressure. Our models are consistent with mass cases from Ramirez & Kaltenegger (2016) that also use the Padova catalog ($\geq 1 M_{\odot}$).

Model planet atmospheres at the Earth-equivalent distance orbiting evolved stars (see Figures 4 and 5) produce lower amounts of ozone but higher amounts of methane than on present-day Earth, which should maintain the detectability of both gases in combination as a sign of biological activity on a planet. The N_2O levels are similar, while the CH_3Cl levels are similar to slightly higher in the model atmosphere of Earth-like planets orbiting post-MS stars receiving similar irradiation than Earth does from our Sun.

Lower ozone production results in higher amounts of UVC reaching the surface of our model planets (see Figures 4 and 5). However, planets on orbits that maximize the overall time in the post-MS HZ spend extended periods of time close to the outer edge of the post-MS HZ, with less incident UVC flux and UVC surface levels comparable to present-day Earth (Figures 6 and 7).

Although the HZ timescales for post-MS stars may not be sufficient for life to develop and evolve, increased luminosity levels cause the post-MS HZ to move past the system’s original frost line, potentially melting previously icy planets or moons to reveal subsurface life. In addition, the wider separation of post-MS HZs results in a larger host-planet apparent angular separation, making them interesting targets for direct imaging with upcoming large telescopes, extending the search for habitable planets to older planetary

systems.

We thank our anonymous referee for their comments that made our manuscript clearer. L.K. and T.K. acknowledge support from the Simons Foundation (SCOL # 290357, Kaltenegger) and the Carl Sagan Institute. T.K. was additionally funded by a NASA Space Grant Fellowship.

REFERENCES

- Baud, B., & Habing, H. J. 1983, *A&A*, 127, 73
- Barnes, R., & Heller, R. 2013, *Astrobiology*, 13, 279
- Bertelli, G., Nasi, E., Girardi, L., & Marigo, P. 2009, *A&A*, 508, 355
- Bertelli, G., Girardi, L., Marigo, P., & Nasi, E. 2008, *A&A*, 484, 815
- Canto, J., & Raga, A. C. 1991, *ApJ*, 372, 646
- Chapman, S. A. (1930) *Theory of Upper-Atmospheric Ozone*, *Mem. R. Met. Soc.*, 3, 26, pp 103-125
- Danchi, W. C., & Lopez, B. 2013, *ApJ*, 769, 27
- Furnes, H., Banerjee, N. R., Muehlenbachs, K., Staudigel, H., & de Wit, M. 2004, *Science*, 304, 578
- Gaia Collaboration, Prusti, T., de Bruijne, J. H. J., et al. 2016, *A&A*, 595, A1
- Haqq-Misra, J. D., Domagal-Goldman, S. D., Kasting, P. J., & Kasting, J. F. 2008, *Astrobiology*, 8, 1127
- Jones, M. I., Jenkins, J. S., Bluhm, P., Rojo, P., & Melo, C. H. F. 2014, *A&A*, 566, A113
- Kaltenegger, L. 2017, *ARA&A*, 55, 433
- Kaltenegger, L., & Haghighipour, N. 2013, *ApJ*, 777, 165
- Kaltenegger, L. 2010, *ApJ*, 712, L125
- Kane, S. R., & Hinkel, N. R. 2013, *ApJ*, 762, 7
- Kasting, J. F., Whitmire, D. P., & Reynolds, R. T. 1993, *Icarus*, 101, 108
- Kasting, J. F., & Ackerman, T. P. 1986, *Science*, 234, 1383
- Kasting, J. F., Holland, H. D., Pinto, J. P. 1985, *J. Geophys. Res.* 90, 10497-10510
- Kopparapu, R. K., Ramirez, R. M., SchottelKotte, J., et al. 2014, *ApJ*, 787, L29
- Kopparapu, R. K., Ramirez, R., Kasting, J. F., et al. 2013, *ApJ*, 765, 131
- Kozakis, T., Kaltenegger, L., & Hoard, D. W. 2018, *ApJ*, 862, 69
- Leconte, J., Forget, F., Charnay, B., et al. 2013, *A&A*, 554, A69
- Lopez, B., Schneider, J., & Danchi, W. C. 2005, *ApJ*, 627, 974
- Luck, R. E. 2015, *AJ*, 150, 88
- O'Malley-James, J. T., & Kaltenegger, L. 2017, *MNRAS*, 469, L26
- Pavlov, A. A., & Kasting, J. F. 2002, *Astrobiology*, 2, 27

- Pavlov, A. A., Kasting, J. F., Brown, L. L., Rages, K. A., & Freedman, R. 2000, *J. Geophys. Res.*, 105, 11981
- Pickles, A. J. 1998, *PASP*, 110, 863
- Quanz, S. P., Crossfield, I., Meyer, M. R., Schmalzl, E., & Held, J. 2015, *International Journal of Astrobiology*, 14, 279
- Ramirez, R. M. 2018, *Geosciences*, 8, 280
- Ramirez, R. M., & Kaltenegger, L. 2018, *ApJ*, 858, 72
- Ramirez, R. M., & Kaltenegger, L. 2017, *ApJ*, 837, L4
- Ramirez, R. M., & Kaltenegger, L. 2016, *ApJ*, 823, 6
- Ramirez, R. M., & Kaltenegger, L. 2014, *ApJ*, 797, L25
- Reimers, D. 1975, *Problems in stellar atmospheres and envelopes.*, 229
- Rugheimer, S., & Kaltenegger, L. 2018, *ApJ*, 854, 19
- Rugheimer, S., Kaltenegger, L., Segura, A., Linsky, J., & Mohanty, S. 2015, *ApJ*, 809, 57
- Rugheimer, S., Segura, A., Kaltenegger, L., & Sasselov, D. 2015, *ApJ*, 806, 137
- Rugheimer, S., Kaltenegger, L., Zsom, A., Segura, A., & Sasselov, D. 2013, *Astrobiology*, 13, 251
- Segura, A., Meadows, V. S., Kasting, J. F., Crisp, D., & Cohen, M. 2007, *A&A*, 472, 665
- Segura, A., Kasting, J. F., Meadows, V., et al. 2005, *Astrobiology*, 5, 706
- Segura, A., Krelove, K., Kasting, J. F., et al. 2003, *Astrobiology*, 3, 689
- Stern, S. A. 2003, *Astrobiology*, 3, 317
- Stock, S., Reffert, S., & Quirrenbach, A. 2018, *A&A*, 616, A33
- Toon, O. B., McKay, C. P., Ackerman, T. P., & Santhanam, K. 1989, *J. Geophys. Res.*, 94, 16287
- Turbet, M., Forget, F., Head, J. W., & Wordsworth, R. 2017, *Icarus*, 288, 10
- Vassiliadis, E., & Wood, P. R. 1993, *ApJ*, 413, 641
- Wolf, E. T. 2018, *ApJ*, 855, L14
- Wolszczan, A., & Frail, D. A. 1992, *Nature*, 355, 145